OPEN ACCESS
Journal of Multidisciplinary Applied Natural Science Vol. 6 No. 3 (2026) https://doi.org/10.47352/jmans.2774-3047.465
Check for updates
Research Article

LC–HRMS-Guided Network Pharmacology Reveals PARP1-Targeting Phytochemicals from *Zanthoxylum acanthopodium* with Anti-Melanoma Activity

Linda Chiuman*, Dewi Purnama, Chrismis Novalinda Ginting, Ermi Girsang, Hariyadi Dharmawan Syahputra, and Iksen Iksen

Received : February 27, 2026	Revised : April 15, 2026	Accepted : May 8, 2026	Online : July 29, 2026

Abstract
Melanoma is an aggressive skin cancer with frequent therapeutic resistance, highlighting the need for multi-target discovery strategies. In this study, an integrative workflow combining LC–HRMS metabolite profiling, network pharmacology, structure-based modeling, and phenotypic evaluation was applied to explore the anti-melanoma potential of *Zanthoxylum acanthopodium* ethanol extract (ZAE). LC–HRMS analysis followed by ADMET-guided screening prioritized 12 candidate metabolites representing diverse structural classes. Integration of transcriptomic datasets, GeneCards targets, and compound-based predictions identified eight consensus genes, with poly(ADP-ribose) polymerase 1 (PARP1) emerging as the top hub within the protein–protein interaction network. Functional enrichment analysis highlighted pathways associated with DNA damage response and apoptosis-related signaling. Molecular docking against the PARP1 catalytic domain suggested favorable binding profiles for several prioritized metabolites, and molecular dynamics simulation supported stable interaction behavior under dynamic conditions. *In vitro* anticancer evaluation in A375 melanoma cells demonstrated concentration-dependent reduction in viability (IC_{50} = 128.03 ± 10.17 µg/mL, 24 h) accompanied by apoptosis-associated nuclear alterations. Overall, this study provides a chemically informed, systems-level framework indicating that ZAE-derived metabolites may influence melanoma cell survival through PARP1-centered stress and apoptosis signaling, offering a foundation for future target validation and structure-guided optimization.

Keywords: apoptosis, LC–HRMS, melanoma, network pharmacology, PARP1, *Zanthoxylum acanthopodium*

1. INTRODUCTION

Melanoma is one of the most aggressive forms of skin cancer, characterized by rapid metastatic progression and a persistent capacity to evade therapeutic pressure [1]. Although advances in targeted therapies and immune checkpoint inhibitors have improved patient survival, treatment resistance and tumor heterogeneity continue to limit durable responses [2]. Increasing attention has therefore shifted toward understanding melanoma through the lens of interconnected molecular networks rather than single-gene paradigms. In particular, signaling pathways associated with DNA damage response and cellular stress adaptation have emerged as important components of melanoma biology, reflecting the dynamic balance between genomic instability and tumor survival [3].

Natural products remain a valuable source of structurally diverse small molecules with potential anticancer activity [4][5]. Modern metabolomics approaches, especially liquid chromatography–high-resolution mass spectrometry (LC-HRMS), enable comprehensive profiling of phytochemical constituents at the molecular level, allowing more rational exploration of plant-derived compounds beyond conventional extract-based assays [6]. However, many natural product studies remain largely descriptive, focusing on cytotoxicity without establishing a broader systems-level context. Integrating metabolite identification with computational strategies provides an opportunity to connect chemical diversity with disease-associated molecular networks and prioritize compounds for further investigation [7].

Network pharmacology has emerged as a useful framework for exploring the complex interactions between multi-component natural products and biological systems [8][9]. By combining transcriptomic datasets, disease-related databases, and in silico target prediction, this approach facilitates the identification of key nodes within signaling networks that may contribute to therapeutic responses [10]. When complemented by structure-based methods such as molecular docking

Table 1. LC–HRMS-based annotation of putative metabolites identified from the ZAE.

No	Name	Formula	Annot. Delta Mass [ppm]	Calc. MW	RT [min]	Area	Compound Classification
M1	Kinsenoside	$C_{10}H_{16}O_8$	1.06	264.0848	3.674	143644576.4	Glycoside
M2	Taxa-4(20),11(12)-dien-5α-ol	$C_{20}H32O$	1.25	288.24568	14.367	89465704.14	Terpenoid
M3	1,2-Bis(3,4-dimethoxyphenyl)propane-1,3-diol	$C_{19}H_{24}O_6$	1.18	348.1577	6.927	56832292.78	Phenol
M4	Laurixamine	$C_{15}H_{33}NO$	0.73	243.25639	8.501	35369374.56	Alkaloid
M5	(−)-α-Cedrene	$C_{15}H_{24}$	0.85	204.18797	11.032	21372704.79	Terpenoid
M6	Certonardosterol J	$C_{29}H_{50}O_4$	1.02	462.37138	16.589	9358165.532	Steroid
M7	Beta-sanshool	$C_{16}H_{25}NO$	0.80	247.19381	10.565	7116496.773	Alkaloid
M8	Capsi-amide	$C_{17}H_{35}NO$	0.92	269.27211	13.187	6316299.697	Alkaloid
M9	Excavatolide M	$C_{24}H_{34}O_{10}$	0.63	482.2155	5.857	5762608.582	Terpenoid
M10	Conicasterol B	$C_{29}H_{44}O$	0.98	408.33962	17.006	4911211.091	Steroid
M11	9-Hydroxy-2,10,10-trimethyltricyclo[6.3.0.0(1,5)]undec-6-ene-6-carboxylic acid	$C_{15}H_{22}O_3$	0.60	250.15704	8.152	4145349.506	Terpenoid
M12	3,4',5-Trihydroxystilbene	$C_{14}H_{12}O_3$	1.03	228.07888	7.134	1611158.387	Aromatic Polyphenol

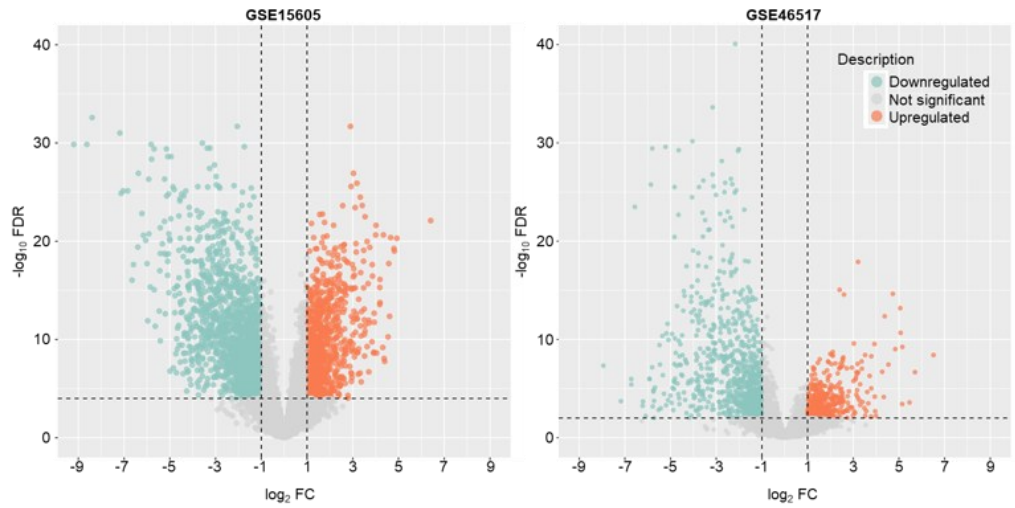

Figure 1. Differential gene expression analysis from melanoma transcriptomic datasets (GSE15605 and GSE46517). Volcano plots illustrating significantly upregulated and downregulated genes based on $\log_2$ fold change and adjusted p-value thresholds. Orange dots represent upregulated genes, cyan green dots indicate downregulated genes, and grey dots denote non-significant transcripts.

and molecular dynamics simulations, network pharmacology allows evaluation of protein–ligand interactions within a mechanistic hypothesis-generating framework [5][11]. Rather than defining definitive molecular mechanisms, such integrative analyses help prioritize candidate targets and guide downstream experimental validation.

Zanthoxylum acanthopodium, a Southeast Asian medicinal plant widely used in traditional culinary and herbal practices, contains a variety of terpenoids, alkaloids, and phenolic compounds that have attracted attention for potential pharmacological activities [12]. Previous investigations have primarily reported general antioxidants or cytotoxic effects, with limited exploration of how its phytochemical components may interact with disease-related signaling networks [12]–[15]. A systematic strategy combining metabolite profiling, computational target prioritization, and biological evaluation is therefore needed to better understand its potential relevance in melanoma research.

In this context, the present study sought to explore the potential relevance of *Z. acanthopodium* ethanolic extract (ZAE) within melanoma-associated molecular networks by integrating metabolite profiling with network-guided computational analysis. Public transcriptomic resources and target prediction strategies were applied to identify highly connected nodes, highlighting poly(ADP-ribose) polymerase 1 (PARP1) as a candidate linked to DNA damage response signaling. Rather than defining a definitive molecular mechanism, structure-based modeling and phenotypic assays were used to examine whether ZAE-derived phytochemicals could interact with this network context and exert measurable effects in melanoma cells. Through this integrative approach, the study aims to provide a systems-level framework for prioritizing natural-product-derived compounds and generating mechanistic hypotheses for future validation.

2. MATERIALS AND METHODS

2.1. Materials

Fruits of ZA were harvested from Berastagi, Karo Regency, North Sumatra, Indonesia during September 2025. Plant authentication was performed and deposited for reference. The collected fruits were dried at 50 °C for approximately 5–7 days, pulverized into fine powder, and kept at ambient temperature.

2.2. Methods

2.2.1. Preparation of Ethanolic Extract of ZA

The ZAE was obtained following our previously reported procedure with minor modifications [16]. Briefly, dried fruit powder was subjected to

maceration using 96% ethanol (Sigma-Aldrich, St. Louis, MO, USA) at a material-to-solvent ratio of 1:10 (w/v). The mixture was kept at room temperature with intermittent agitation to enhance solvent penetration and metabolite extraction. The extract was subsequently filtered to remove solid residues, and the filtrate was concentrated under reduced pressure using a rotary evaporator to obtain the crude ethanolic extract. The extraction yield was 6.4% (w/w), calculated based on the dry weight of the starting plant material. The resulting extract was stored at 4 °C in airtight containers until further chemical and biological analyses.

2.2.2. LC–HRMS Metabolite Profiling

LC–HRMS analysis of ZAE was performed following our previously established protocol with minor adaptations [6]. Briefly, powdered samples were extracted using HPLC-grade methanol (Sigma -Aldrich, St. Louis, MO, USA), vortexed, and filtered through a 0.20 µm nylon membrane prior to analysis. Chromatographic separation was carried out on a Vanquish Horizon UHPLC system (Thermo Fisher Scientific, USA) equipped with an Accucore phenyl-hexyl column maintained at 40 °C. A binary mobile phase consisting of water and acetonitrile, each containing 0.1% formic acid, was applied under a gradient elution program. Mass spectrometric detection was conducted using an Orbitrap Exploris 240 operating in positive ion mode with data-dependent MS/MS acquisition. High-resolution full-scan spectra were acquired across the m/z 70–1000 range, and fragmentation spectra were obtained using stepped collision energies. Raw data processing and compound annotation were performed in Compound Discoverer 3.3 using mzCloud, ChemSpider, LipidMaps, and curated in-house mass lists. Detailed instrumental settings and gradient conditions have been reported previously [6].

2.2.3. Differential Gene Expression and Disease-Associated Target Identification

Melanoma transcriptomic profiles were obtained from the Gene Expression Omnibus database [17], including datasets GSE15605 [18] and GSE46517 [19]. Differential gene expression between melanoma and normal tissues was evaluated using the limma package implemented in R. Genes were considered significantly altered when they satisfied both an adjusted p-value < 0.05 and an absolute $\log_2$ fold change ≥ 1, thereby capturing transcripts showing either increased or decreased expression [20]. To complement transcriptome-derived candidates with curated disease information, melanoma-associated genes were additionally retrieved from the GeneCards database [21]. Only entries with a relevance score ≥ 10 were retained to enrich for targets with stronger documented links to melanoma biology.

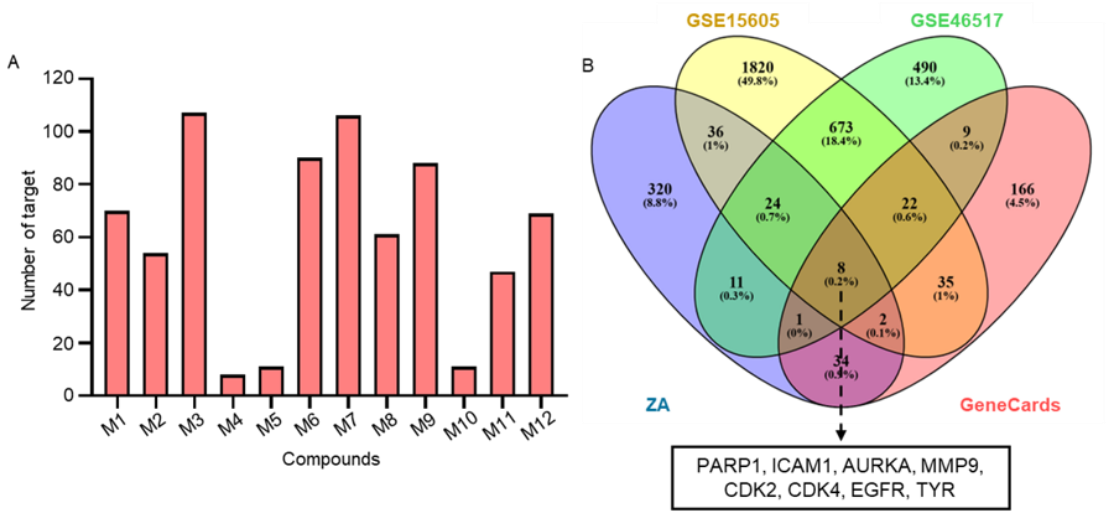

Figure 2. Integration of compound-associated targets with melanoma-related genes. (a) Number of predicted protein targets for each prioritized metabolite (M1–M12). (b) Venn diagram showing the eight overlap targets between compound-associated targets (ZA), differentially expressed genes from GSE15605 and GSE46517, and melanoma-related genes retrieved from the GeneCards database.

2.2.4. Target Identification of LC–HRMS-Derived Metabolites from ZAE

Metabolites detected from LC–HRMS profiling of ZAE were subjected to a multi-step filtering strategy prior to target prediction. Initially, annotated features were curated to exclude non-metabolite signals and compounds lacking natural product relevance. Only candidates with mass error < 2.5 ppm were retained to ensure reliable metabolite annotation [6]. The remaining compounds were further screened for drug-likeness and pharmacokinetic suitability using SwissADME [22], where molecules satisfying Lipinski's rule of five were prioritized [6][20]. Additional physicochemical and predicted ADME parameters were evaluated to remove candidates with unfavorable pharmacokinetic profiles. The filtered compound list was subsequently submitted to SwissTargetPrediction [23] to estimate potential protein targets based on chemical similarity and probabilistic modeling. Predicted targets from all prioritized metabolites were combined and duplicates were removed to generate a non-redundant compound–target dataset.

2.2.5. Protein–Protein Interaction (PPI) Network Construction, Hub Gene Identification, and Functional Enrichment Analysis

Melanoma-associated genes derived from differential expression analysis (GSE15605 and GSE46517), GeneCards mining, and predicted targets of LC–HRMS-identified ZAE metabolites were first integrated through intersection analysis using an online Venn diagram generator to obtain consensus candidates supported across multiple datasets. The overlapping targets were subsequently imported into the STRING database (https://string-db.org) to evaluate potential protein–protein interactions [24]. Network data were retrieved in CSV format using a minimum interaction confidence score of 0.7 to ensure high-confidence associations. The resulting interaction network was visualized and further analyzed using Cytoscape software [25]. Hub gene prioritization was performed with the CytoHubba plugin [26] employing the Edge Percolated Component (EPC) algorithm, which ranks nodes based on network stability and topological importance. Genes with higher EPC scores were considered central nodes within the PPI network and selected for downstream functional and structural analyses. Functional enrichment analysis was subsequently performed to investigate the biological roles of the identified targets. Gene Ontology (GO) annotation and Kyoto Encyclopedia of Genes and Genomes (KEGG) pathway enrichment analyses were conducted using the online bioinformatics platform (https://www.bioinformatics.com.cn/). GO enrichment covered three categories, including biological process (BP), cellular component (CC), and molecular function (MF). Enriched pathways and functional terms with adjusted p-values < 0.05 were considered statistically significant. The top enriched GO terms and KEGG pathways were visualized using the integrated visualization tools provided by the platform.

2.2.6. Clinical Expression Analysis and Survival Evaluation

PARP1 protein expression in normal skin and melanoma tissues was examined using immunohistochemistry data obtained from the Human Protein Atlas (HPA) database [27]. Representative images were selected based on antibody validation status and staining quality to enable qualitative comparison of expression patterns between normal and tumor samples. Differences in staining intensity and subcellular localization were visually assessed to illustrate relative PARP1 expression. The clinical relevance of PARP1 expression was further evaluated using survival data derived from The Cancer Genome Atlas (TCGA) cohort [28]. Kaplan–Meier survival analysis was performed through publicly available online platforms integrating TCGA transcriptomic datasets. Patients were stratified into high- and low-expression groups according to the median PARP1 expression level, and overall survival differences were assessed using the log-rank test. Hazard ratios (HR) and corresponding p-values were reported as provided by the analysis platform [29].

2.2.7. Molecular Docking and Dynamic Simulation

Structure-based evaluation of prioritized ZAE metabolites was performed by molecular docking against the human PARP1 catalytic domain (PDB ID: 4R6E) obtained from the RCSB Protein Data Bank. Protein preparation followed our previously

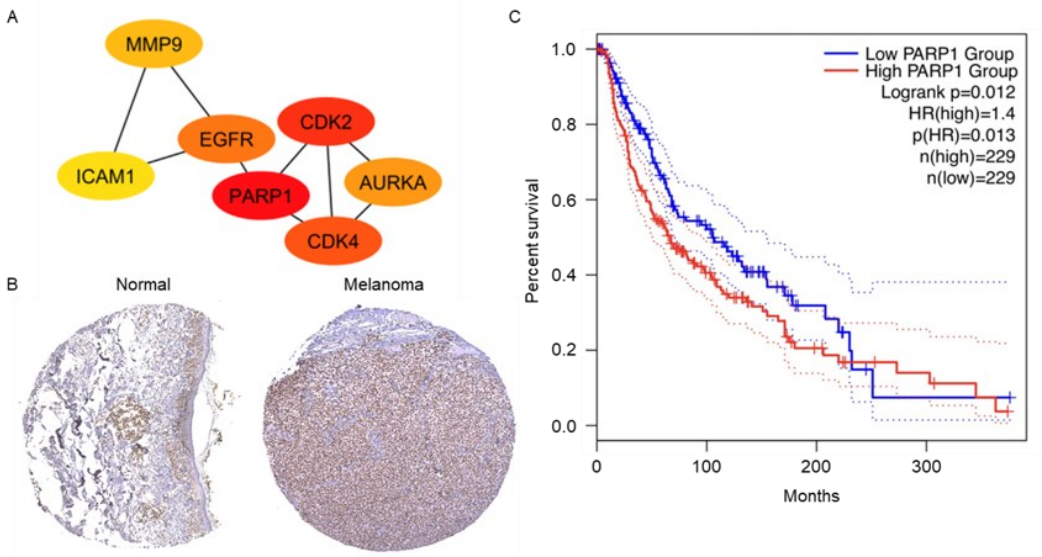

Figure 3. Network topology and clinical relevance of PARP1 within the melanoma-associated target network. (a) Protein–protein interaction (PPI) network of the intersecting genes with EPC-based node ranking. (b) Representative immunohistochemistry (IHC) images of PARP1 staining in normal skin and melanoma tissues. (c) Kaplan–Meier survival analysis comparing high- and low-PARP1 expression groups.

described workflow with minor modifications [5], [30], including removal of co-crystallized ligands, ions, and solvent molecules and assignment of protonation states prior to PDBQT conversion. Docking protocol reliability was confirmed by redocking the native inhibitor niraparib into the catalytic pocket. Ligand structures derived from LC–HRMS screening were geometry-optimized before docking. Virtual screening was conducted using AutoDock Vina with a grid center at X = −69.232, Y = 22.94, and Z = 26.733 and a grid size of 12 × 14 × 14 Å covering the NAD^+ catalytic region. Docked complexes were ranked based on binding energy and ligand efficiency, and the top-scoring complex was selected for subsequent molecular dynamics simulation. Molecular dynamic simulations were performed using GROMACS 2021.7 with the CHARMM36 force field, following a protocol adapted from our earlier report [6]. Each protein–ligand complex was solvated in a TIP3P water model and neutralized with counterions prior to energy minimization. Equilibration was performed under NVT and NPT ensembles, followed by a 100 ns production run to evaluate structural stability. Trajectory analyses focused on backbone root mean square deviation (RMSD), ligand RMSD, radius of gyration (Rg), residue flexibility (RMSF), and hydrogen bond formation to assess interaction persistence within the PARP1 catalytic pocket.

2.2.8. Cell Culture

The human melanoma cell line A375 was obtained from the American Type Culture Collection (ATCC, Manassas, VA, USA). Cells were maintained in Dulbecco's Modified Eagle Medium (DMEM) supplemented with 10% fetal bovine serum (FBS) and 1% penicillin–streptomycin. Cultures were incubated at 37 °C in a humidified atmosphere containing 5% CO_2. All cell culture reagents and supplements were purchased from GIBCO (Grand Island, NY, USA). Cells were routinely monitored to ensure stable morphology and confluency prior to experimental treatments.

2.2.9. Cell Viability Assay

Cell viability was assessed using the 3-(4,5-dimethylthiazol-2-yl)-2,5-diphenyltetrazolium bromide (MTT) colorimetric assay following a protocol adapted from our previous study with minor modifications [29]. ZAE was initially dissolved in dimethyl sulfoxide (DMSO) to prepare a 200 mg/mL stock solution and subsequently diluted in complete culture medium to the indicated working concentrations. The final DMSO concentration was kept constant across all treatment

groups and maintained at a non-cytotoxic level. Control cells received the corresponding volume of vehicle alone. Briefly, A375 cells were seeded in 96 -well plates at a density of 8 × 10^3 cells per well and allowed to adhere overnight before treatment with increasing concentrations of ZAE for 24 h. Subsequently, MTT solution (500 µg/mL; Sigma-Aldrich, St. Louis, MO, USA) was added and incubated for 3 h to permit formazan formation. The crystals were solubilized in dimethyl sulfoxide and absorbance was recorded at 570 nm using a VICTOR3/Wallac 1420 microplate reader (PerkinElmer, Waltham, MA, USA). Half-maximal inhibitory concentration (IC_{50}) values were determined by nonlinear regression analysis using GraphPad Prism version 8 (GraphPad Software, San Diego, CA, USA). Each treatment condition was analyzed in six technical replicate wells within each experiment, and the assay was repeated in at least three independent biological experiments.

2.2.10. Apoptosis Analysis by Hoechst 33342 Staining

Apoptotic nuclear morphology was evaluated using Hoechst 33342 staining following previous report [31]. A375 melanoma cells were seeded in 96-well plates at a density of 8 × 10^3 cells per well in 100 µL complete culture medium and allowed to attach overnight. Treatment solutions were prepared from the same ZAE stock solution described above. Cells were then treated with increasing concentrations of ZAE ranging from 0 to 100 µg/mL for 24 h. After treatment, cells were incubated with 10 µM Hoechst 33342 (Sigma-Aldrich, St. Louis, MO, USA) for 15 min at 37 °C in the dark. Nuclear morphology was observed using a fluorescence microscope (ECLIPSE Ts2; Nikon, New York, NY, USA), and images were captured. Apoptotic cells exhibiting condensed or fragmented chromatin were quantified from three randomly selected microscopic fields per well and expressed as a percentage of total cells. Quantification was performed in three independent biological experiments.

2.2.11. Statistical Analysis

All experimental data are presented as mean ± SD from at least three independent biological experiments. In the MTT assay, each treatment condition was analyzed in six technical replicate wells within each experiment. For the Hoechst 33342 apoptosis assay, apoptotic nuclei were

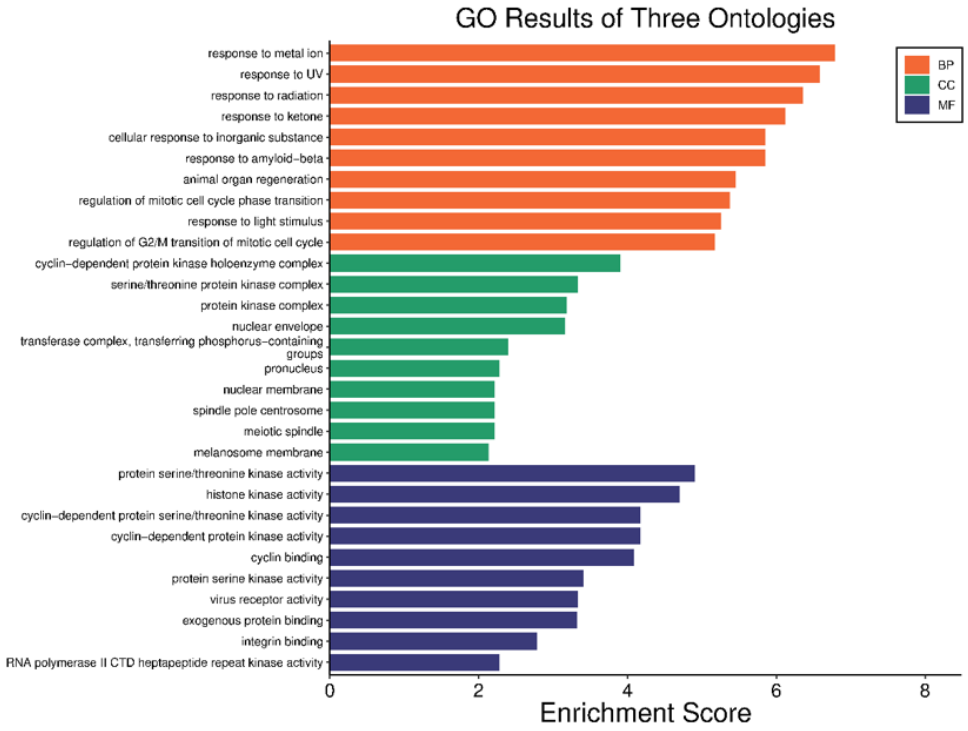

Figure 4. GO enrichment analysis of core targets.

quantified across three independent biological experiments. Statistical analyses were performed using GraphPad Prism version 8 (GraphPad Software, San Diego, CA, USA). Differences among groups were evaluated using one-way analysis of variance (ANOVA) followed by Tukey's post hoc multiple comparison test. A value of $p < 0.05$ was considered statistically significant.

3. RESULTS AND DISCUSSIONS

3.1. LC–HRMS-based Metabolite Profiling and Prioritization of Candidate Phytochemicals

Chemical profiling of the ZAE was performed using LC–HRMS to characterize the metabolite composition prior to computational investigation. The total ion chromatogram displayed numerous signals distributed across the retention time range, reflecting the chemical complexity of the extract (Figure S1). Automated peak detection identified a total of 228 measurable features within the acquired mass spectrum, suggesting the presence of structurally diverse constituents. Putative metabolite annotation was conducted through accurate mass matching and database comparison. To refine the dataset, detected compounds were subjected to physicochemical and pharmacokinetic filtering. Selection criteria were based on Lipinski's rule of five alongside ADMET-related parameters to prioritize molecules with acceptable drug-like properties [32][33]. This filtering step yielded twelve annotated compounds that satisfied the predefined drug-likeness and ADMET criteria. The detailed ADMET prediction parameters supporting compound prioritization are provided in Table S1. For clarity in subsequent analyses, the prioritized metabolites were assigned simplified identifiers (M1–M12) according to their order of detection and annotation. The selected molecules represented diverse structural classes, including glycosides, terpenoids, alkaloids, steroids, and phenolic derivatives, with representative examples such as kinsenoside, β-sanshool, conicasterol B, excavatolide M, and resveratrol (Table 1). The prioritized compounds exhibited molecular weights ranging from approximately 200 to 480 Da, while mass deviations remained within acceptable analytical limits, supporting reliable annotation. Variations in retention time further suggested differences in polarity and structural characteristics among the identified metabolites [34]. These candidates were subsequently advanced to network pharmacology and structure-based analyses.

3.2. Identification of Disease-associated and Compound-related Targets

To identify candidate targets associated with melanoma and ZA-derived metabolites, transcriptomic datasets, curated disease databases, and compound-related targets were systematically integrated. Differential gene expression analysis of two independent melanoma datasets revealed a total of 1,238 differentially expressed genes in GSE46517, including 805 upregulated and 433 downregulated genes, while 2,620 differentially expressed genes were identified in GSE15605, comprising 1,074 upregulated and 1,546 downregulated genes (Figure 1). These gene sets were used to represent melanoma-associated transcriptional alterations. To complement transcriptomic evidence with curated disease information, melanoma-related genes were retrieved from the GeneCards database. An initial pool of 8,640 genes was obtained and further refined by applying a relevance score threshold (≥ 10), resulting in 277 disease-associated targets included for subsequent integration.

In parallel, potential protein targets corresponding to the prioritized metabolites (M1–M12) were predicted using publicly available target prediction resources. The number of predicted targets varied among individual compounds, ranging from 8 to 107 targets per metabolite (Figure 2(a)). After removing duplicate entries, a total of 436 unique compound-related targets were retained. The gene sets derived from GSE46517, GSE15605, GeneCards, and compound target prediction were subsequently integrated to identify consensus candidates supported across multiple data sources. Intersection analysis identified eight overlapping genes shared among all four datasets, including PARP1, intercellular adhesion molecule 1 (ICAM1), aurora kinase A (AURKA), matrix metallopeptidase 9 (MMP9), cyclin-dependent kinase 2 (CDK2), cyclin-dependent kinase 4 (CDK4), epidermal growth factor receptor (EGFR), and tyrosinase (TYR) (Figure 2(b)). These common targets were subsequently carried forward for

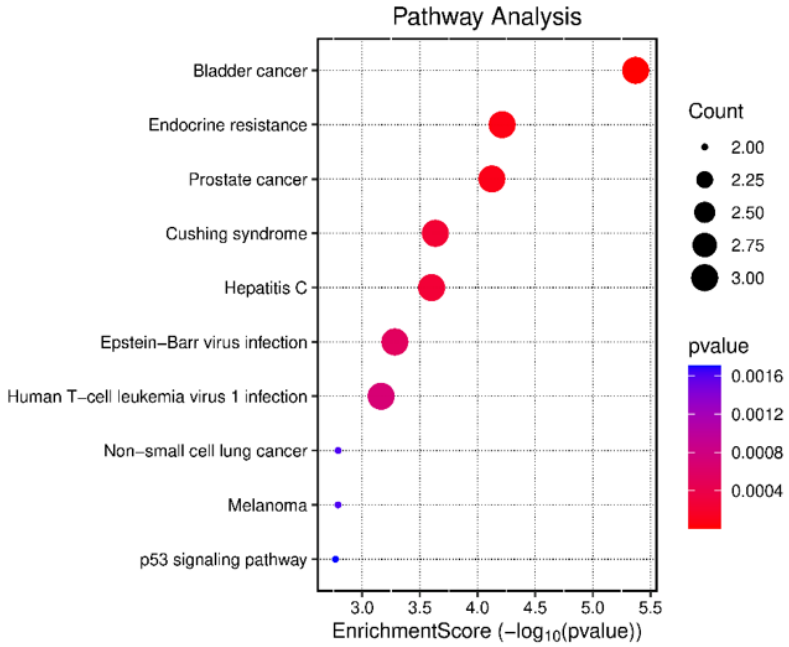

Figure 5. KEGG pathway enrichment analysis of core targets.

protein–protein interaction network construction and downstream functional enrichment analysis.

3.3. PPI Network Construction and Clinical Relevance Analysis

To further explore the functional relationships and potential clinical relevance of the genes identified through integrative analysis, PPI network analysis was performed. The eight intersecting genes obtained from the previous step (PARP1, ICAM1, AURKA, MMP9, CDK2, CDK4, EGFR, and TYR) were subjected to PPI network construction to evaluate potential functional associations. Under the selected interaction confidence threshold, seven genes formed a connected network, whereas TYR remained unlinked, indicating limited direct interactions within the analyzed context (Figure 3(a)). The resulting network revealed a cluster comprising signaling molecules, DNA damage–related proteins, and regulators associated with cellular stress responses, including EGFR, PARP1, CDK2, CDK4, AURKA, MMP9, and ICAM1. This connectivity suggests potential involvement in coordinated regulatory processes linked to tumor progression. Hub gene prioritization using the CytoHubba plugin and Edge Percolated Component (EPC) algorithm ranked PARP1 as the top node within the network, followed by CDK2, CDK4, and EGFR. EPC scoring reflects node stability within the network topology, indicating that PARP1 occupies a central position connecting multiple signaling components. PARP1 is a key regulator of DNA damage repair and chromatin remodeling, and increased PARP1 expression has been reported in melanoma tissues compared with normal melanocytes [35]. Experimental studies have shown that PARP1 overexpression can enhance DNA repair efficiency and promote resistance to apoptosis-inducing stress [35][36], whereas pharmacological inhibition of PARP1 has been associated with increased DNA damage accumulation, elevated apoptotic signaling, and reduced tumor cell survival in melanoma models [37][38]. In addition, PARP1 has been implicated in regulating oxidative stress responses and modulating transcriptional programs linked to tumor adaptation, supporting its potential involvement in cancer progression [39]. These reported biological roles are consistent with the central network position of PARP1 observed in the present analysis.

To further evaluate the clinical relevance of this hub gene, PARP1 protein expression was examined by IHC comparing normal skin and melanoma tissues. Representative images revealed distinct differences in PARP1 staining patterns between normal skin and melanoma samples (Figure 3(b)).

Normal skin displayed relatively weak and localized nuclear staining with preserved tissue architecture and recognizable structural layering. In contrast, melanoma tissue exhibited increased cellular density accompanied by stronger and more diffuse nuclear PARP1 staining across tumor cells. These observations are consistent with elevated PARP1 expression in melanoma compared with normal skin [36]. Survival analysis was subsequently performed to assess the association between PARP1 expression and patient outcomes. Kaplan–Meier curves demonstrated a statistically significant difference in overall survival between high- and low-expression groups (log-rank p = 0.012; HR = 1.4) (Figure 3(c)), with higher PARP1 expression corresponding to reduced survival probability. Although causality cannot be inferred from this analysis, the observed association suggests potential clinical relevance of PARP1 expression in melanoma prognosis. Collectively, the PPI topology and clinical data highlight PARP1 as a central node within the identified network and support its inclusion for subsequent mechanistic validation.

3.4. Functional Enrichment Analysis of Intersecting Targets

To further characterize the biological roles associated with the intersecting genes, GO and KEGG enrichment analyses were performed. The GO analysis revealed that the identified targets were significantly enriched in biological processes related to cellular stress responses, including responses to metal ions, ultraviolet radiation, and external stimuli, together with regulation of mitotic transition and signaling-associated processes (Figure 4). These enriched biological terms suggest that the identified genes may participate in cellular adaptation mechanisms under stress conditions commonly observed in tumor microenvironments. Within the cellular component category, enriched terms were mainly associated with protein kinase complexes, nuclear-associated structures, and transferase-related assemblies, indicating potential involvement in intracellular signaling and transcriptional regulation. Molecular function analysis further highlighted enrichment in kinase-related activities, including protein serine/threonine kinase activity, histone kinase activity, and cyclin-dependent protein kinase activity, supporting a role in regulatory signaling cascades rather than structural functions. The complete enrichment outputs for GO biological process, molecular function, and cellular component analyses are provided in Tables S2 – S4 for transparency and detailed interpretation.

KEGG pathway enrichment analysis demonstrated significant association with several cancer-related pathways, including bladder cancer, endocrine resistance, prostate cancer, and melanoma-associated signaling pathways, as well as the p53 signaling pathway (Figure 5). These pathways are widely linked with DNA damage response, cellular stress signaling, and apoptosis

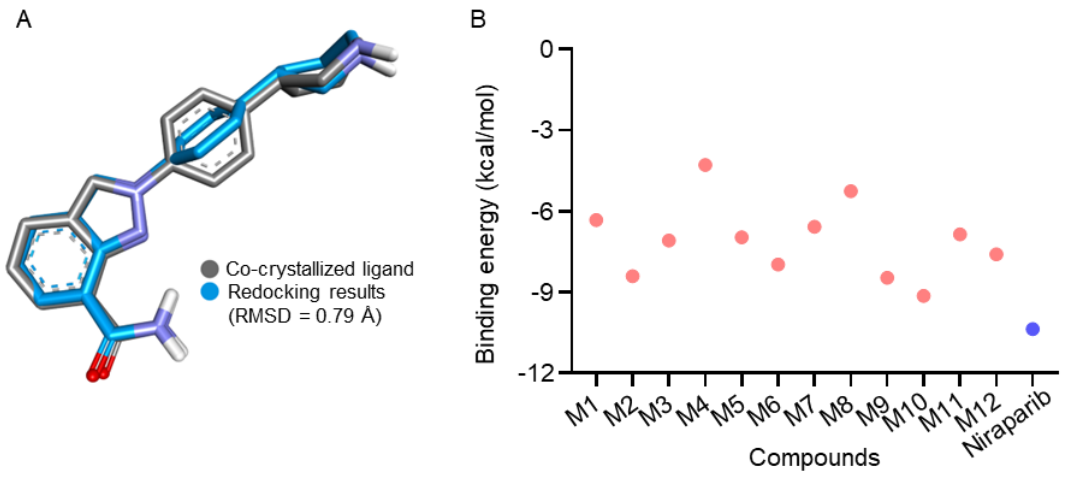

Figure 6. Docking analysis of ZA-derived metabolites targeting the PARP1 catalytic domain. (a) Redocking validation (RMSD = 0.79 Å). (b) Binding energy comparison of M1–M12.

regulation. The enrichment of melanoma and p53-related pathways is consistent with the network topology and clinical relevance analysis, suggesting that the identified targets may converge on signaling networks involved in tumor stress adaptation. Notably, PARP1 is a well-established regulator of DNA damage sensing and apoptosis-associated signaling, particularly through modulation of p53-mediated pathways and cellular stress responses [3][40]. Although enrichment analysis does not indicate direct mechanistic causation, the observed pathway patterns highlight apoptosis-related signaling as a biologically relevant context associated with the identified hub targets. The complete enrichment outputs for KEGG pathway analyses are provided in Table S5 for transparency and detailed interpretation.

3.5. Molecular Docking of Prioritized Metabolites against the PARP1 Catalytic Domain

To investigate the potential structural interaction between prioritized ZA-derived metabolites and the hub target identified from integrative analysis, molecular docking simulations were conducted using the human PARP1 catalytic domain. The crystal structure of PARP1 co-crystallized with the clinically approved inhibitor niraparib was selected to accurately represent the NAD^+ binding pocket responsible for enzymatic activity. Prior to screening, the docking protocol was validated through redocking of the native ligand, which reproduced the crystallographic pose with an RMSD value of 0.79 Å (Figure 6(a)), indicating reliable docking performance. Predicted binding energies varied among metabolites M1–M12, suggesting different interaction propensities within the catalytic pocket (Figure 6(b)). For comparison, niraparib was also docked under the same conditions and exhibited a binding energy of −10.366 kcal/mol, serving as a reference control for the screened metabolites. Among the ZA-derived compounds, M10 exhibited the lowest docking energy (−9.136 kcal/mol), followed by M9 (−8.467 kcal/mol), M2 (−8.41 kcal/mol), M6 (−7.974 kcal/mol), M12 (−7.6 kcal/mol), and M3 (−7.086 kcal/mol). Moderate docking scores were observed for M5 (−6.965 kcal/mol), M11 (−6.857 kcal/mol), M7 (−6.576 kcal/mol), and M1 (−6.323 kcal/mol), whereas M8 (−5.255 kcal/mol) and M4 (−4.283 kcal/mol) displayed comparatively weaker predicted affinities. Overall, several metabolites were predicted to occupy the catalytic cleft with energetically favorable docking poses, although their predicted binding affinities remained lower than that of the reference inhibitor niraparib.

The docking results suggest that several metabolites are positioned within the catalytic region corresponding to the niraparib-binding pocket, consistent with structural characteristics of PARP1 inhibitors targeting the NAD^+ catalytic site. PARP1 is a key regulator of poly(ADP-ribosyl)ation during the DNA damage response, and perturbation of this catalytic domain has been associated with impaired DNA repair signaling and enhanced apoptotic susceptibility in melanoma-related contexts. In melanoma, PARP-related pathways have also been implicated in therapeutic response and resistance, further supporting the biological relevance of PARP1 as a target within stress-adaptive tumor signaling [41]. Although docking analysis alone cannot confirm functional inhibition, the predicted binding profiles provide structural support for potential modulation of PARP1-associated pathways highlighted in the preceding network and enrichment analyses. While none of the screened metabolites surpassed niraparib in predicted binding affinity, several compounds—particularly M10, M9, and M2—demonstrated relatively favorable docking scores and may still represent structurally relevant natural-product-derived scaffolds for further optimization. Taken together, these results suggest that several ZA-derived metabolites may interact favorably with the PARP1 catalytic domain. Based on docking ranking, M10 was selected for subsequent molecular dynamics simulation, as it exhibited the lowest predicted binding energy among the ZA-derived metabolites. Given the computational cost of molecular dynamic simulations, focusing on this top-ranked complex enabled further evaluation of binding stability and interaction persistence over time.

3.6. Molecular Dynamics Simulation of the M10 – PARP1 Catalytic Domain Complex

To further evaluate the dynamic stability of the top-ranked docking complex, molecular dynamics (MD) simulation was performed for the M10–

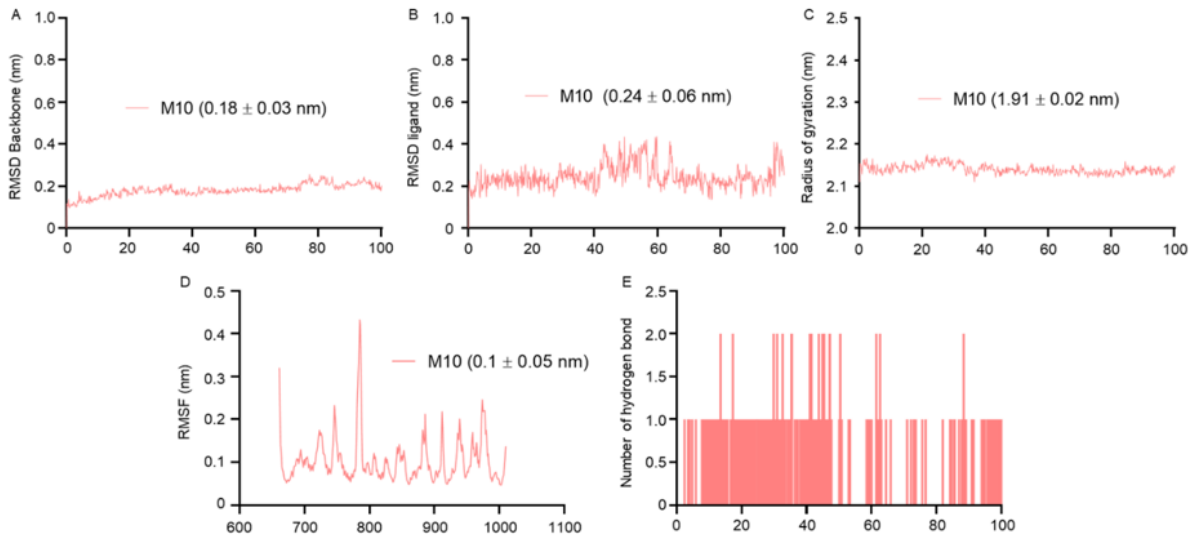

Figure 7. Molecular dynamics simulation analysis of the M10–PARP1 catalytic domain complex. (a) Backbone RMSD of PARP1. (b) Ligand RMSD of M10. (c) Radius of gyration. (d) Residue flexibility (RMSF). (e) Hydrogen bond occupancy during the simulation.

PARP1 catalytic domain system. Structural stability was assessed through backbone deviation, ligand movement, protein compactness, residue flexibility, and hydrogen bond interactions over the simulation trajectory. The backbone RMSD of PARP1 rapidly increased during the initial equilibration phase (0–10 ns), rising from approximately 0.10 to 0.18 nm, and subsequently stabilized within a narrow range of 0.17–0.23 nm for the remainder of the simulation (Figure 7(a)). Minor fluctuations were observed around 70–90 ns but did not exceed 0.25 nm, indicating preservation of the overall catalytic domain structure after ligand binding. The ligand RMSD profile showed slightly higher variability compared with the protein backbone (Figure 7(b)). After an initial adjustment phase during the first 15 ns, the ligand RMSD fluctuated mainly between 0.20 and 0.40 nm. A transient increase was observed around 40–60 ns, where values approached 0.45 nm, followed by re-stabilization toward the later stages of the simulation. These patterns suggest conformational rearrangement within the catalytic pocket rather than ligand dissociation. The Rg analysis demonstrated minimal structural expansion or compaction of the protein (Figure 7(c)). Rg values remained relatively constant between 2.13 and 2.16 nm throughout the 100 ns trajectory, with only minor oscillations observed between 20 and 40 ns, indicating maintained global compactness of the PARP1 catalytic domain.

Residue-level flexibility assessed by RMSF revealed that most residues exhibited fluctuations below 0.15 nm, while higher peaks reaching 0.30–0.45 nm were primarily localized in loop regions around residues 700–820 and near the C-terminal segment (Figure 7(d)). The catalytic core displayed comparatively low mobility, suggesting that ligand binding did not induce major instability within the functional region. Hydrogen bond analysis showed intermittent formation of approximately 0–2 hydrogen bonds during the simulation (Figure 7(e)). Hydrogen bond occupancy appeared more frequent during the early to mid-phase (10–50 ns), with shorter transient contacts observed toward the later time points. Although not continuously maintained, these recurring interactions suggest dynamic stabilization of M10 within the catalytic cleft. Collectively, the molecular dynamic trajectories indicate that the M10–PARP1 complex reached structural equilibrium after the early simulation phase and maintained overall stability without significant conformational disruption. Given the central role of the PARP1 catalytic domain in DNA damage signaling and apoptosis-related pathways, the observed stability supports the potential of M10 to engage this region under dynamic conditions.

3.7. Phenotypic Validation in A375 Melanoma Cells

To evaluate the phenotypic response associated with targets identified through integrative analyses, A375 melanoma cells were treated with increasing concentrations of ZAE for 24 h, followed by assessment of cell viability using an MTT assay. ZAE exposure resulted in a concentration-dependent reduction in metabolic activity (Figure 8 (a)). Nonlinear regression analysis indicated an IC_{50} value of 128.03 ± 10.17 µg/mL after 24 h treatment, suggesting moderate antiproliferative activity within the tested range.

To determine whether decreased viability was associated with apoptosis-related nuclear alterations, Hoechst 33342 (H33342) staining was performed. Fluorescence microscopy revealed progressive nuclear condensation and chromatin fragmentation in treated cells compared with untreated controls (Figure 8(b)). These morphological changes became more evident with increasing ZAE concentration, characterized by brighter and punctate nuclear signals. Quantification of apoptotic nuclei demonstrated a dose-dependent increase in apoptotic populations (Figure 8(c)). While low concentrations produced modest effects, treatment at 50 and 100 µg/mL significantly elevated the proportion of apoptotic cells relative to control. The observed nuclear changes are consistent with apoptosis-associated chromatin remodeling, in agreement with enrichment results highlighting stress-response and apoptosis-related pathways potentially associated with PARP1 signaling.

Although ZAE represents a complex mixture of metabolites, the phenotypic response observed after 24 h exposure provides experimental support that ZA-derived constituents may influence apoptosis-associated processes in melanoma cells. In agreement with the observed apoptotic morphology, previous studies have reported apoptosis induction by ZA-derived fractions in melanoma models [13]. A recent study demonstrated that the ethyl acetate fraction induced apoptosis in B16F10 melanoma cells through increased caspase-3 expression and dose-dependent cytotoxicity, with an IC_{50} value of approximately 249.3 µg/mL [13]. In comparison, the present study employed a human melanoma model and revealed a lower IC_{50} value (128.03 ± 10.17 µg/mL) together with clear nuclear condensation patterns detected by Hoechst 33342 staining, suggesting enhanced apoptotic sensitivity under the tested conditions. While the previous work primarily focused on phenotypic apoptosis endpoints, the current study integrates LC-HRMS, network pharmacology, clinical relevance analysis, molecular docking, and molecular dynamics simulations targeting PARP1, thereby providing a mechanistically informed framework that helps contextualize phytochemical activity within DNA-damage response pathways. Since ZAE is a crude extract containing multiple phytochemical constituents, the observed cytotoxic activity is likely attributable to the combined or potentially synergistic effects of several metabolites rather than a single dominant compound. This may partly explain the moderate IC_{50} value observed in the

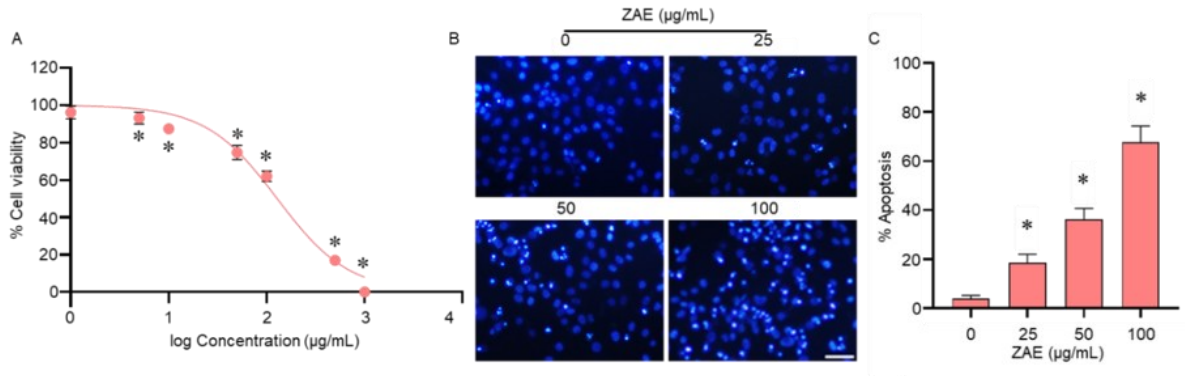

Figure 8. Phenotypic validation of ZAE in A375 melanoma cells after 24 h treatment. (a) Dose–response curve showing reduced cell viability and calculated IC_{50}. (b) Representative Hoechst 33342 nuclear staining images indicating apoptosis-related morphological changes. (c) Quantification of apoptotic cells following ZAE exposure. *$p < 0.05$ vs control. Scale bar is 10 µm.

present study. Future investigations should focus on the isolation of individual bioactive compounds or the enrichment of specific fractions to better define their relative contributions and underlying mechanisms of action.

Taken together, the present study combines LC–HRMS-based metabolite profiling with integrative network pharmacology, clinical relevance analysis, and structure-guided modeling to delineate a PARP1-centered framework potentially involved in melanoma-associated stress and apoptosis signaling. The LC–HRMS screening enabled prioritization of ZA-derived metabolites that were subsequently linked to disease-relevant targets through transcriptomic and protein interaction analyses, providing a chemically informed basis for downstream structural evaluation. Molecular docking and dynamic simulations further supported the compatibility of selected metabolites within the PARP1 catalytic domain, while phenotypic assays in A375 cells demonstrated apoptosis-associated nuclear alterations following extract exposure. Compared with previous studies that primarily described cytotoxic or apoptotic effects of ZA at the phenotypic level, the present work integrates chemical characterization with computational and cellular evidence, offering a more mechanistically resolved perspective on ZA-derived activity. Although direct target engagement remains to be experimentally confirmed, this multi-layered strategy highlights ZA-derived metabolites as potential modulators of melanoma cell survival and provides a foundation for future structure-guided optimization and mechanistic investigation.

4. CONCLUSIONS

This study presents an integrative framework combining LC–HRMS-based metabolite profiling, network pharmacology, clinical relevance analysis, and structure-guided modeling to explore the potential anti-melanoma activity of ZA extract. The multi-layered strategy enabled identification of PARP1-associated signaling as a plausible axis linking ZA-derived metabolites to stress-response and apoptosis-related pathways, while molecular docking and dynamic simulations supported structural compatibility within the PARP1 catalytic domain. Phenotypic evaluation in A375 melanoma cells further demonstrated apoptosis-associated nuclear alterations following extract exposure, providing complementary biological context to the computational findings. Rather than establishing a definitive mechanism, the present work offers a chemically informed and systems-level perspective that may guide future studies toward target validation, compound optimization, and deeper mechanistic investigation of ZA-derived phytochemicals in melanoma research.

AUTHOR INFORMATION

Corresponding Author

Linda Chiuman — Department of Medicine, Universitas Prima Indonesia, Medan-20118 (Indonesia);
orcid.org/0000-0003-4822-0099
Email: lindachiuman@unprimdn.ac.id

Authors

Dewi Purnama — Doctoral Programme of Medicine, Universitas Prima Indonesia, Medan-20118 (Indonesia);
orcid.org/0009-0001-7227-3230

Chrismis Novalinda Ginting — Department of Medicine, Universitas Prima Indonesia, Medan-20118 (Indonesia);
orcid.org/0000-0003-2269-2717

Ermi Girsang — Department of Medicine, Universitas Prima Indonesia, Medan-20118 (Indonesia);
orcid.org/0000-0003-4313-4941

Hariyadi Dharmawan Syahputra — Department of Clinical Pharmacy, Universitas Prima Indonesia, Medan 20118, Medan-20118 (Indonesia);
orcid.org/0000-0003-1090-8859

Iksen Iksen — Department of Pharmacy, Universitas Senior Medan, Medan-20141 (Indonesia);
orcid.org/0000-0003-0166-4792

Author Contributions

Conceptualization, L. C. and I. I.; Methodology, Validation, Resources, Data Curation, Writing – Original Draft Preparation, Funding Acquisition, L. C., D. P., H. D. S., and I. I.; Software, I. I.; Formal Analysis, Investigation, L. C., D. P., C. N. G., E.

G., H. D. S., and I. I.; Writing – Review & Editing, L. C., H. D. S., and I. I.; Visualization, Supervision, L. C. and I. I.; Project Administration, L. C., and H. D. S.

Conflicts of Interest

The authors declare no conflict of interest.

SUPPORTING INFORMATION

Supplementary data associated with this article can be found in the online version at doi: 10.47352/jmans.2774-3047.465

ACKNOWLEDGEMENT

This research supported by the Universitas Prima Indonesia and Universitas Senior Medan.

DECLARATION OF GENERATIVE AI

Not applicable.

REFERENCES

[1] C. Caraviello, G. Nazzaro, G. Tavoletti, F. Boggio, N. Denaro, G. Murgia, E. Passoni, V. B. Mancin, and A. V. Marzano. (2025). "Melanoma Skin Cancer: A Comprehensive Review of Current Knowledge". *Cancers.* **17** (17). 10.3390/cancers17172920.

[2] S. J. Hachey and A. D. Boiko. (2016). "Therapeutic Implications of Melanoma Heterogeneity". *Experimental Dermatology.* **25** (7): 497-500. 10.1111/exd.13002.

[3] L. Maresca, B. Stecca, and L. Carrassa. (2022). "Novel Therapeutic Approaches with DNA Damage Response Inhibitors for Melanoma Treatment". *Cells.* **11** (9). 10.3390/cells11091466.

[4] Iksen, W. Witayateeraporn, B. Hardianti, and V. Pongrakhananon. (2024). "Comprehensive Review of Bcl-2 Family Proteins in Cancer Apoptosis: Therapeutic Strategies and Promising Updates of Natural Bioactive Compounds and Small Molecules". *Phytotherapy Research.* **38** (5): 2249-2275. 10.1002/ptr.8157.

[5] Iksen, N. Singharajkomron, H. M. Nguyen, H. N. T. Hoang, D. V. Ho, and V. Pongrakhananon. (2024). "Adunctin E from Conamomum rubidum Induces Apoptosis in Lung Cancer via HSP90AA1 Modulation: A Network Pharmacology and In Vitro Study". *International Journal of Molecular Sciences.* **25** (21). 10.3390/ijms252111368.

[6] Iksen, F. N. Manihuruk, H. D. Syahputra, M. Saragih, I. E. E. Manurung, R. S. U. Peranginangin, D. F. P. Saragih, H. A. Simanjuntak, and K. Gurning. (2026). "Integrative Multi-Omics and Experimental Approaches Identify SRC as a Central Target of Garcinia atroviridis Flavonoids in Lung Cancer". *Journal of Multidisciplinary Applied Natural Science.* **6** (1): 540-552. 10.47352/jmans.2774-3047.344.

[7] X. Jiang, Z. Xu, H. Wang, H. Wang, J. Zhao, N. Maihemuti, S. Jiang, M. Xiao, K. Zhang, S. Liang, Y. Shi, and K. Wang. (2025). "Metabolomics and Integrated Network Pharmacology Analysis Revealed Multi-Targeted Anti-Cancer Effect of FuZhengXiaoJi Decoction Against Non-Small Cell Lung Cancer". *Phytomedicine.* **143** : 156855. 10.1016/j.phymed.2025.156855.

[8] P. Zhang, D. Zhang, W. Zhou, L. Wang, B. Wang, T. Zhang, and S. Li. (2023). "Network Pharmacology: Towards the Artificial Intelligence-Based Precision Traditional Chinese Medicine". *Briefings in Bioinformatics.* **25** (1). 10.1093/bib/bbad518.

[9] R. Islamie, Iksen, B. C. Buana, K. Gurning, H. D. Syahputra, and H. S. Winata. (2022). "Construction of Network Pharmacology-Based Approach and Potential Mechanism from Major Components of Coriandrum sativum L. Against COVID-19". *Pharmacia.* **69** (3): 689-697. 10.3897/pharmacia.69.e84388.

[10] J. F. Wijaya, L. Chiuman, H. D. Syahputra, V. E. Kaban, R. Razoki, C. N. Ginting, and I. Iksen. (2025). "Investigation of Potential Molecular Targets of Zanthoxylum acanthopodium in Ovarian Cancer Using Network Pharmacology Assessments". *Journal of Multidisciplinary Applied Natural Science.* **5** (2): 630-643. 10.47352/

jmans.2774-3047.268.

[11] Q. Ma, Y. Liu, Q. Zhang, W. Yi, Y. Sun, X. Gao, X. Zhao, H. Wang, K. Lei, and W. Luo. (2024). "Integrating Network Pharmacology, Molecular Docking and Experimental Verification to Reveal the Mechanism of Artesunate in Inhibiting Choroidal Melanoma". *Frontiers in Pharmacology.* **15** : 1448381. 10.3389/fphar.2024.1448381.

[12] I. Syaputri, E. Girsang, and L. Chiuman. (2022). "Test of Antioxidant and Antibacterial Activity of Ethanol Extract of Andaliman Fruit (Zanthoxylum acanthopodium DC.) with DPPH (1,1-Diphenyl-2-Picrylhydrazyl) Trapping Method and Minimum Inhibitory Concentration". *International Journal of Health and Pharmaceutical.* **2** (2): 215-224. 10.51601/ijhp.v2i2.36.

[13] E. R. Megawati, H. Bangun, I. B. Putra, and M. Rusda. (2025). "Cytotoxicity and Apoptotic Effects of the Ethyl Acetate Fraction of Zanthoxylum acanthopodium DC. Fruit on B16F10 Melanoma Cell Culture". *Contemporary Oncology.* **29** (4): 354-359. 10.5114/wo.2025.155773.

[14] D. Satria, J. Silalahi, G. Haro, S. Ilyas, and P. A. Z. Hasibuan. (2019). "Cell Cycle Inhibition of Ethyl Acetate Fraction of Zanthoxylum acanthopodium DC. Fruit Against T47D Cells". *Open Access Macedonian Journal of Medical Sciences.* **7** (5): 726-729. 10.3889/oamjms.2019.178.

[15] D. M. Syari, R. Rosidah, P. A. Z. Hasibuan, G. Haro, and D. Satria. (2019). "Evaluation of Cytotoxic Activity of Alkaloid Fractions of Zanthoxylum acanthopodium DC. Fruits". *Open Access Macedonian Journal of Medical Sciences.* **7** (22): 3745-3747. 10.3889/oamjms.2019.495.

[16] S. M. Sinaga, G. Haro, S. Sudarmi, and Iksen. (2019). "Phytochemical Screening and Antihyperglycemic Activity of Ethanolic Extract of Coriandrum sativum L. Leaf". *Rasayan Journal of Chemistry.* **12** (4): 1992-1996. 10.31788/RJC.2019.1245451.

[17] T. Barrett, S. E. Wilhite, P. Ledoux, C. Evangelista, I. F. Kim, M. Tomashevsky, K. A. Marshall, K. H. Phillippy, P. M. Sherman, M. Holko, A. Yefanov, H. Lee, N. Zhang, C. L. Robertson, N. Serova, S. Davis, and A. Soboleva. (2013). "NCBI GEO: Archive for Functional Genomics Data Sets—Update". *Nucleic Acids Research.* **41** (Database Issue): D991-D995. 10.1093/nar/gks1193.

[18] L. Raskin, D. R. Fullen, T. J. Giordano, D. G. Thomas, M. L. Frohm, K. B. Cha, J. Ahn, B. Mukherjee, T. M. Johnson, and S. B. Gruber. (2013). "Transcriptome Profiling Identifies HMGA2 as a Biomarker of Melanoma Progression and Prognosis". *Journal of Investigative Dermatology.* **133** (11): 2585-2592. 10.1038/jid.2013.197.

[19] O. Kabbarah. (2010). "Integrative Genome Comparison of Primary and Metastatic Melanomas". *PLoS ONE.* **5** (5): e10770. 10.1371/journal.pone.0010770.

[20] Iksen and B. C. Buana. (2022). "Identification of Potential COVID-19 Targets and Pathways Derivate from Various Phenolic Compounds from Chives (Allium schoenoprasum) by Using Network Pharmacology Approach". *Media Pharmaceutica Indonesiana.* **4** (2): 157-167. 10.24123/mpi.v4i2.5272.

[21] G. Stelzer, N. Rosen, I. Plaschkes, S. Zimmerman, M. Twik, S. Fishilevich, T. I. Stein, R. Nudel, I. Lieder, Y. Mazor, S. Kaplan, D. Dahary, D. Warshawsky, Y. Guan -Golan, A. Kohn, N. Rappaport, M. Safran, and D. Lancet. (2016). "The GeneCards Suite: From Gene Data Mining to Disease Genome Sequence Analyses". *Current Protocols in Bioinformatics.* **54**. 10.1002/cpbi.5.

[22] A. Daina, O. Michielin, and V. Zoete. (2017). "SwissADME: A Free Web Tool to Evaluate Pharmacokinetics, Drug-Likeness and Medicinal Chemistry Friendliness of Small Molecules". *Scientific Reports.* **7** : 42717. 10.1038/srep42717.

[23] A. Daina, O. Michielin, and V. Zoete. (2019). "SwissTargetPrediction: Updated Data and New Features for Efficient Prediction of Protein Targets of Small Molecules". *Nucleic Acids Research.* **47** (W1): W357-W364. 10.1093/nar/gkz382.

[24] D. Szklarczyk, K. Nastou, M. Koutrouli, R.

Kirsch, F. Mehryary, R. Hachilif, D. Hu, M. E. Peluso, Q. Huang, T. Fang, N. T. Doncheva, S. Pyysalo, P. Bork, L. J. Jensen, and C. von Mering. (2025). "The STRING Database in 2025: Protein Networks with Directionality of Regulation". *Nucleic Acids Research.* **53** (D1): D730-D737. 10.1093/nar/gkae1113.

[25] P. Shannon, A. Markiel, O. Ozier, N. S. Baliga, J. T. Wang, D. Ramage, N. Amin, B. Schwikowski, and T. Ideker. (2003). "Cytoscape: A Software Environment for Integrated Models of Biomolecular Interaction Networks". *Genome Research.* **13** (11): 2498-2504. 10.1101/gr.1239303.

[26] C. H. Chin, S. H. Chen, H. H. Wu, C. W. Ho, M. T. Ko, and C. Y. Lin. (2014). "CytoHubba: Identifying Hub Objects and Sub-Networks from Complex Interactome". *BMC Systems Biology.* **8** (Suppl 4): S11. 10.1186/1752-0509-8-S4-S11.

[27] P. J. Thul and C. Lindskog. (2018). "The Human Protein Atlas: A Spatial Map of the Human Proteome". *Protein Science.* **27** (1): 233-244. 10.1002/pro.3307.

[28] K. Chang, C. J. Creighton, C. Davis, L. A. Donehower, J. Drummond, D. R. Wheeler, and A. Ally. (2013). "The Cancer Genome Atlas Pan-Cancer Analysis Project". *Nature Genetics.* **45** (10): 1113-1120. 10.1038/ng.2764.

[29] Iksen, N. Singharajkomron, A. Wongtayan, O. Wattanathamsan, A. Choonhapan, S. Wademonkolgorn, H. M. Nguyen, T. H. X. Hoang, H. T. Nguyen, and V. Pongrakhananon. (2026). "Unveiling the Antimetastatic Activity and Molecular Mechanism of Montanine in Lung Cancer Cells via the Integration of Network Pharmacology Approaches with In Vitro and In Vivo Investigations". *Journal of Integrative Medicine.* 10.1016/j.joim.2026.01.001.

[30] H. D. Syahputra, M. Masfria, P. A. Z. Hasibuan, and Iksen. (2022). "In Silico Docking Studies of Phytosterol Compounds Selected from Ficus religiosa as Potential Chemopreventive Agent". *Rasayan Journal of Chemistry.* **15** (2): 1080-1084. 10.31788/RJC.2022.1526801.

[31] Iksen, S. Sinsook, O. Wattanathamsan, K. Buaban, S. Chamni, and V. Pongrakhananon. (2022). "Target Identification of 22-(4-Pyridinecarbonyl) Jorunnamycin A, a Tetrahydroisoquinoline Derivative from the Sponge Xestospongia sp., in Mediating Non-Small-Cell Lung Cancer Cell Apoptosis". *Molecules.* **27** (24): 8948. 10.3390/molecules27248948.

[32] L. Z. Benet, C. M. Hosey, O. Ursu, and T. I. Oprea. (2016). "BDDCS, the Rule of 5 and Drugability". *Advanced Drug Delivery Reviews.* **101** : 89-98. 10.1016/j.addr.2016.05.007.

[33] A. Reichel and P. Lienau. (2016). "Pharmacokinetics in Drug Discovery: An Exposure-Centred Approach to Optimising and Predicting Drug Efficacy and Safety". *Handbook of Experimental Pharmacology.* **232** : 235-260. 10.1007/164_2015_26.

[34] E. M. Novoa-Del-Toro and M. Witting. (2024). "Navigating Common Pitfalls in Metabolite Identification and Metabolomics Bioinformatics". *Metabolomics.* **20** (5): 103. 10.1007/s11306-024-02167-2.

[35] P. Donizy, C. Wu, J. Mull, M. Fujimoto, A. Chłopik, Y. Peng, S. C. Shalin, M. A. Selim, S. Puig, M. Fernandez-Figueras, C. R. Shea, W. Biernat, J. Ryś, A. Marszalek, and M. P. Hoang. (2020). "Up-Regulation of PARP1 Expression Significantly Correlated with Poor Survival in Mucosal Melanomas". *Cells.* **9** (5): 1135. 10.3390/cells9051135.

[36] P. Kupczyk. (2021). "PARP1 as a Marker of an Aggressive Clinical Phenotype in Cutaneous Melanoma: A Clinical and an In Vitro Study". *Cells.* **10** (2): 286. 10.3390/cells10020286.

[37] P. Kupczyk, A. Simiczyjew, J. Marczuk, E. Dratkiewicz, A. Beberok, J. Rok, M. Pieniazek, P. Biecek, D. Nevozhay, B. Slowikowski, G. Chodaczek, D. Wrzesniok, D. Nowak, and P. Donizy. (2019). "PARP Inhibitor PJ34 Protects Mitochondria and Induces DNA-Damage Mediated Apoptosis in Combination With Cisplatin or Temozolomide in B16F10 Melanoma Cells". *Frontiers in Physiology.* **10** : 538. 10.3389/

fphys.2019.00538.

[38] F. Fratangelo, R. Camerlingo, M. V. Carriero, G. Pirozzi, G. Palmieri, G. Gentilcore, C. Ragone, M. Minopoli, P. A. Ascierto, and M. L. Motti. (2018). "Effect of ABT-888 on the Apoptosis, Motility and Invasiveness of BRAFi-Resistant Melanoma Cells". *International Journal of Oncology.* **53** (3): 1149-1159. 10.3892/ijo.2018.4457.

[39] M. J. Schiewer, J. F. Goodwin, S. Han, J. C. Brenner, M. A. Augello, J. L. Dean, F. Liu, J. L. Planck, P. Ravindranathan, A. M. Chinnaiyan, P. McCue, L. G. Gomella, G. V. Raj, A. P. Dicker, J. R. Brody, J. M. Pascal, M. M. Centenera, L. M. Butler, W. D. Tilley, and K. E. Knudsen. (2012). "Dual Roles of PARP-1 Promote Cancer Growth and Progression". *Cancer Discovery.* **2** (12): 1134 -1149. 10.1158/2159-8290.CD-12-0120.

[40] Y. Wang, W. Luo, and Y. Wang. (2019). "PARP-1 and Its Associated Nucleases in DNA Damage Response". *DNA Repair.* **81** : 102651. 10.1016/j.dnarep.2019.102651.

[41] J. O. Spiegel, B. Van Houten, and J. D. Durrant. (2021). "PARP1: Structural Insights and Pharmacological Targets for Inhibition". *DNA Repair.* **103** : 103125. 10.1016/j.dnarep.2021.103125.